



Multi-track multi-layer friction stir additive manufacturing of AA6061-T6 alloy

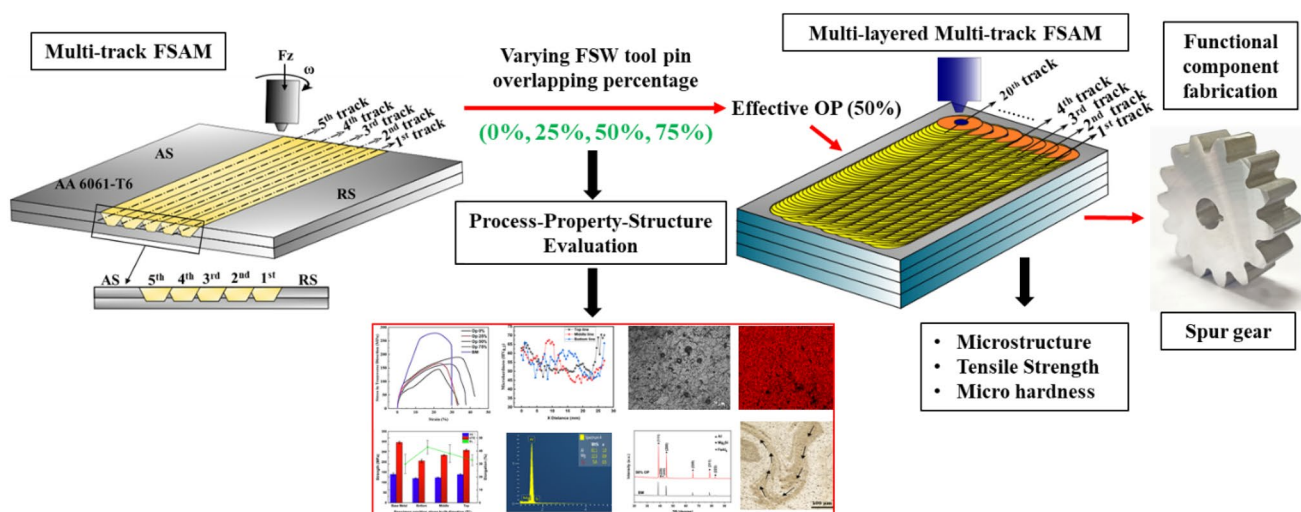
Ankan Das¹ · Tanmoy Medhi¹ · Sajan Kapil¹ · Pankaj Biswas¹

Received: 5 November 2022 / Accepted: 29 June 2023 / Published online: 11 July 2023
© The Author(s), under exclusive licence to Springer Nature Switzerland AG 2023

Abstract

Friction stir additive manufacturing (FSAM) is a solid-state sheet-based metal additive manufacturing (MAM) process that utilizes the classical friction stir welding (FSW) process to join the layers. So far, FSAM has been explored for fabricating thin to thick metallic walls. However, to realize large-scale defect-free dense structures, FSAM demands multiple welding tracks in each layer with a suitable overlap. Therefore, this work investigates the effect of overlapping percentages (0%, 25%, 50%, and 75%) in joining two layers of AA6061-T6 alloy by a concave shouldered tool and a cylindrical taper pin. The multi-track FSAM strategy is incorporated to join the two layers with a raster pattern toolpath. The joined layer's cross-sectional micrographs showed the absence of the half-ellipse-shaped banded patterns and a high degree of plasticized material mixing with an increase in overlapping percentage. It has been noticed that the successive overlapping weld tracks act as a post-heat treatment process for pre-scanned tracks, leading to more heat exposure time and grain re-growth. High magnification images and energy dispersion spectroscopy (EDS) revealed the homogeneous distribution of secondary precipitates into the samples prepared by 50% overlap, resulting in relatively higher tensile strength and uniform hardness. As 50% overlap exhibited better mechanical and microstructural properties, it has been further implemented as a toolpath stepover to join multiple sheets of AA6061-T6 material to create a block. The outcomes showed a dense microstructure in the processed zones and good interlayer bonding with increased tensile strength (maximum UTS 258 MPa) and hardness (maximum value 102 HV_{0.1}) along the building direction. Moreover, a spur gear has been realized by machining from the block created by multi-layered multi-track FSAM.

Graphical Abstract



Keywords Metal additive manufacturing (MAM) · Friction stir lap welding (FSLW) · FSW tool pin overlapping toolpaths · Raster pattern · Multi-track friction stir additive manufacturing (FSAM)

1 Introduction

In recent times, metal additive manufacturing (MAM) is becoming the most transformative approach to industrial production that enables the fabrication of lighter and stronger complex parts directly from a computer-aided design (CAD) model [1]. There are several MAM processes for realizing metallic objects, such as powder bed fusion (PBF) [2], direct energy deposition (DED) [3], sheet lamination (SL) [4], etc., from raw materials such as powder, wire, and sheets, etc. The aluminum-magnesium-silicon alloys (AA6061) show a low strength-to-weight ratio, an ability to improve by aging, good weldability, good specific strength, and high corrosion resistance [5–7]. Therefore, this material is commercially available in all three forms: powders, wires, and sheets. However, joining aluminum alloys by a fusion heat source-based AM technique can severely affect its mechanical and microstructural properties due to hot cracking, warpage, and multiple phase transitional defects [8]. It has been found that in DED, fusion bonding of aluminum alloys triggers the rapid formation of the oxides on particles and between two-layer interfaces [9]. These oxide films are evaporated partially by lasers, typically used during selective laser melting or sintering, which generates microvoids that produce porosity in the fabricated parts [10]. At the same time, the remaining unevaporated oxide particles are trapped in the successive layers or adjacent tracks encountered as a prime cause for structural performance degradation of aluminum components produced by fusion-based AM processes [11]. However, researchers have demonstrated a few non-fusion approaches to foreclose solidification-related defects while processing aluminum alloys using rods and sheets as feedstock [12].

Friction stir welding (FSW) is an efficient and cost-effective alternative to fusion-based welding for AM of aluminum alloys. It is a solid-state joining process that utilizes the frictional heat to plastically deform the material, on the course of stirring effect by the tool pin, intermixes the two pieces of metal, and forges the softened material by mechanical pressure [13]. FSW eliminates the phase transformational defects as it processes under the melting temperature of that substrate [14]. Recently, FSW has been utilized for solid-state AM technologies, such as additive friction stir deposition (AFSD) and friction stir additive manufacturing (FSAM). During AFSD, the material is fed as a solid rod or powder through the middle of an un-consumable rotating tool. Subsequently, deposited

tracks overlap, and previously deposited layers act as a substrate for the next layer. After the complete deposition of a layer, the tool height adjustment is made to accommodate the successive layer [15]. Several researchers have demonstrated this AM approach based on aluminum alloy [16–18] and reported a minor improvement in the alloy's fatigue performance due to the intermetallic dispersion. By exploiting the high compressive shear stresses of AFSD, Jordon et al. [19] and Agrawal et al. [20] demonstrated successful depositions of fully dense AA5083 and Ti-6Al-4 V alloy structures employing recycled machine chips as feedstock material. However, AFSD shows promising results, but a few difficulties may arise during the fabrication of any overhang or hollow sections, which demands an extra support structure. Whereas FSAM is based on the principle of sheet lamination (SL) technology, where each sheet is considered a single layer, and multiple layers are joined through lap/lap-butt joint configuration [21]. The most advantageous part of this process is individual sheet strength, each layer can be handled separately, and no support structure is needed. The FSAM has demonstrated various similar and dissimilar aluminum alloys, showing the recrystallized fine grain structures and homogeneous distribution over the processed area [21–26]. FSAM of aluminum alloys has enhanced the mechanical and microstructural properties of the structural components [24]. FSW is also helpful for microstructural modification by grain refinement and particle dispersion in the case of casting and wrought products [27, 28]. FSAM has shown a route for producing composites and reinforced materials such as polymer-steel laminated [29]. He et al. [30] studied the underwater FSAM on Al-Zn-Mg alloy and showed that water-cooled build has a high degree of supersaturation and age-strengthening ability attributed to a high cooling rate. Liu et al. revealed an innovative approach for intermetallic free large area FSAM of Al-steel bimetallic components through interfacial amorphization [31]. In most of the studies, single-track FSAM has focused on revealing the presence of multiple defects like micro-voids, hooking, and kissing bonds on the advancing side (AS) or retreating sides (RS) of the stirred zone (SZ). These defects lead to micro-crack propagation and, eventually, failure of the fabricated components [23, 24]. More than one welding pass has distinguished outcomes to reduce such detrimental issues [32, 33]. In the case of a multi-track welding strategy, successive track positioning and overlapping shoulder ratio are the most significant criteria [34, 35]. However,

Table 1 Chemicals composition of as received AA 6061-T6 (wt%)

| Si | Mg | Fe | Cu | Cr | Zn | Ti | Mn | Al |
|-----|-----|------|------|------|------|------|------|---------|
| 0.8 | 1.2 | 0.35 | 0.24 | 0.18 | 0.02 | 0.03 | 0.05 | Balance |

Table 2 Mechanical properties of as received AA 6061-T6 substrate

| Properties | Ultimate tensile strength (UTS) | Yield strength (YS) | Percentage elongation (%EL) | Hardness (HV _{0.1}) |
|------------|---------------------------------|---------------------|-----------------------------|-------------------------------|
| Values | 291 MPa | 266 MPa | 15% | 84 |

minimal studies were available in the direction of SZ overlapping and material flow analysis, and no work has been reported yet that incorporates the non-threaded tool pins for multi-track FSAM. Notably, the tool pin overlapping percentage (OP) in multi-track welding strategy is a significant clause associated with FSAM, required for joining a defect-free large cross-sectional area. Therefore, before joining a multi-layered structure by FSAM, it is essential to ascertain the effective tool pin overlapping percentage to join two layers by multi-tracks.

In this work, a systematic investigation has been carried out to understand the effect of different tool pin overlapping percentages to join two wide sheets of AA6061-T6 material by multi-track FSAM. This understanding was then utilized to create a block of the same material by multi-track multi-layer FSAM. The proposed methodology

can be readily extended for exploring the FSAM of new materials.

2 Materials and experimental procedures

2.1 Multi-track FSAM

This study was performed on rolled AA6061-T6 (aluminum-magnesium-silicon alloy) sheets of 200 mm × 150 mm × 4 mm, and the chemical composition and mechanical properties are shown in Tables 1 and 2. Before welding, each sheet surface was cleaned using emery paper and acetone. The experimental setup of the FSAM has been developed in-house by retrofitting a 3-axis vertical milling machine, as shown in Fig. 1a. A flexible clamping fixture was used to hold the sheets, as shown in Fig. 1b. The FSW tool was made of H-13 tool steel, having a hardness of 49 HRC. The tool, shown in Fig. 1c, has a shoulder concavity of 3° and a diameter of 18 mm, with a cylindrical trapper pin of a tip and root diameters of 4 mm and 6 mm, respectively, and a pin height of 5 mm. In this study, a set of trial and error experiments were conducted in order to find the suitable range of rotational speed (450–875 rpm), traverse speed (30–90 mm/min), and tilt angle (1.5°–3°)

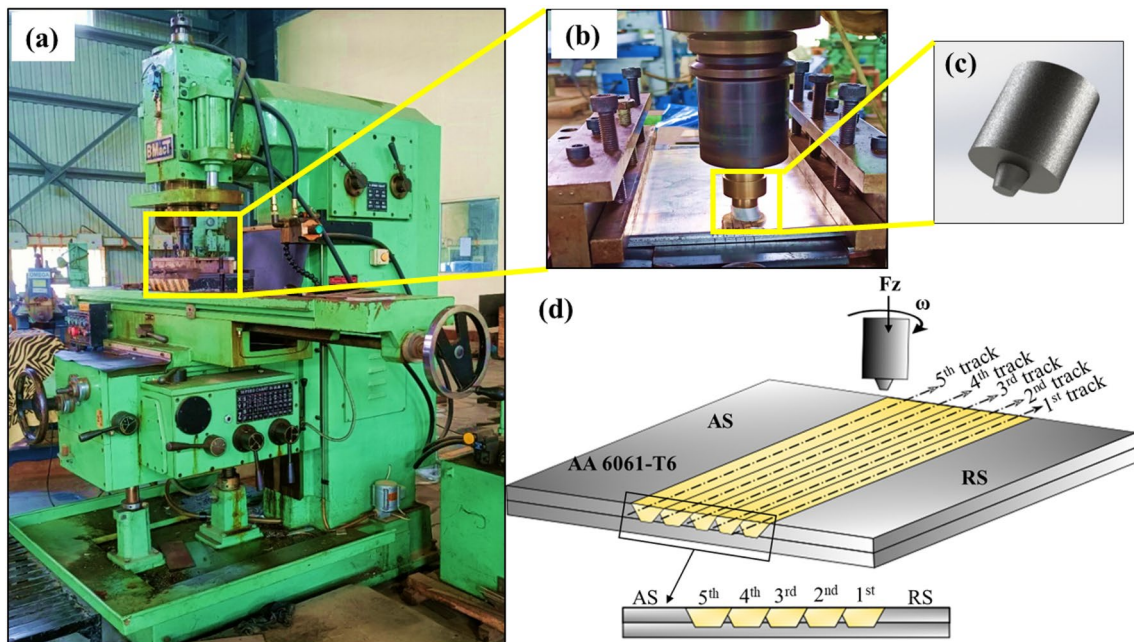


Fig. 1 a Experimental setup for FSAM; b Flexible clamping fixture; c FSW tool; d Overview of two-layer joining

for FSAM. In this range of parameters, single-track welding gave defect-free joining. Therefore, to perform FSAM experiments, the process parameters were selected from the abovementioned range. The tool's rotational speed was maintained at 600 rpm, traverse speed at 66 mm/min; the tool tilt angle was 2.5° , and the plunge depth of the shoulder was set at 0.1 mm. As the width of the sheets to be joined is higher than the tool pin diameter, multiple welding tracks will be required to cover the entire area, as shown in Fig. 1d. For parallel multi-tracks, the tool pin OP can be expressed as,

$$OP = \left[\left(1 - \frac{L}{D} \right) \times 100 \right] \% \quad (1)$$

where L is the centerline distance between two adjacent tracks, and D is the tool pin root diameter.

Four levels of tool pin overlap (viz. 0%, 25%, 50%, and 75%) with five parallel tracks for each case were considered to join the sheets. The next track was performed on the advancing side of the previous one without changing the welding direction, as shown in Figs. 1d and 2a. These welding tracks were performed continuously without any intermediate cooling.

For metallurgical analysis, various specimens were extracted from the weldment by wire-electro discharge machining (W-EDM) from three positions of the processed zone, as shown in Fig. 2d. The samples were prepared by polishing on emery papers of different grades to 2500 grit,

followed by polishing with $0.3 \mu\text{m}$ alumina colloidal solution. The polished samples were etched using modified Keller's reagent (3 mL HCL, 3 mL HNO_3 , 1.5 mL HF, and 40 mL H_2O) 35 s times to reveal the microstructure. The macrostructure and microstructure of the samples were observed using a Stereo zoom microscope and an upright optical microscope, respectively. The grain size was measured in each SZ's top and bottom regions by line-intercept technique as per ASTM E 112–12. Further, a few specimens were analyzed by field emission scanning electron microscopy (FESEM), energy dispersion x-ray spectroscopy (EDS), and x-ray diffraction (XRD) to examine the SZ morphology.

Two types of tensile samples were cut out from the processed area to determine the strength in two particular directions, based on ASTM, B557M-10 standard, as shown in Fig. 2b. One sample is in the longitudinal welding direction, i.e., parallel to toolpaths, and another in the traverse direction, i.e., normal to the toolpaths. Lap-shear tensile specimens were also prepared to check the shear strength, as shown in Fig. 2c. The tensile tests were carried out in a Shimadzu Static UTM machine having a capacity of 100 kN at a strain rate of 1 mm/min. The fractography analysis was carried out by Carl Zeiss Sigma 300 FESEM machine. The micro-hardness was recorded by Omnitest Vickers micro-hardness tester, across the cross-section, on three distinct horizontal lines on the top, middle, and bottom, i.e., on the

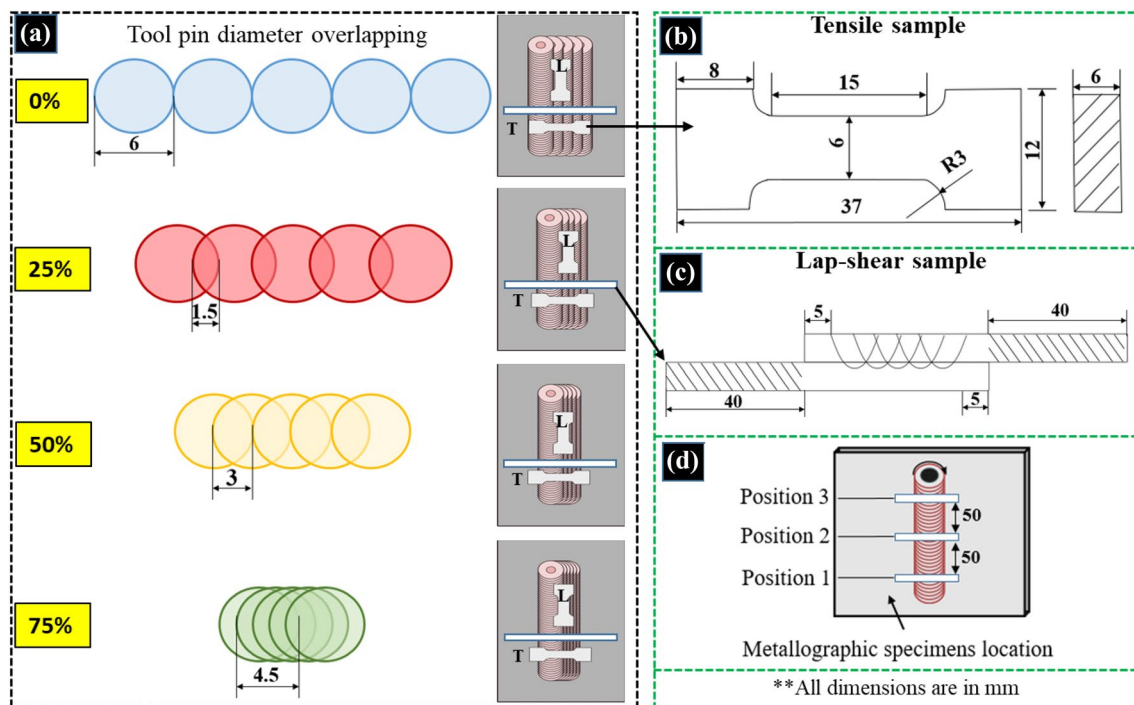


Fig. 2 a Experimental process plan with different pin OP, b tensile sample dimensions, T: specimen in the transverse direction; L: specimen in a longitudinal direction; c Lap-shear tensile samples; d metallographic samples locations

layer interface. The top line was 1 mm below the shoulder-affected surface, and the inter-distance between the three lines was approximately 2 mm. The indentation was made at intervals of 0.5 mm across the three horizontal lines, and the applied load was 100 g for a dwell period of 10 s.

2.2 Multi-layer multi-track FSAM

A multi-layered (four layers) block has been fabricated using AA6061-T6 alloy sheets of 200 mm × 150 mm × 4 mm. A large area has been joined/scanned by an FSW tool. This tool maintains the same dimensional configuration as used earlier in the case of multi-track FSAM. Twenty overlapping welding tracks were performed on each layer, i.e., 60 tracks to fabricate the block. The most effective OP from the previous study has been incorporated into this fabrication process. The schematic illustration of the fabrication process is shown in Fig. 3a. All other process parameters were kept the same as mentioned in Sect. 2.1. An intermediate face milling has been performed to prepare a smooth surface before the new layer joining and at the end of all layer joining, as shown in Fig. 3b. After completion of the multi-layered build, mechanical and microstructural characterization was performed on it to study the nature of material mixing and flow tensile properties and micro-hardness in the build

direction. Here, tensile samples were extracted from the tool track transverse direction and building directions. Tool track transverse direction samples followed ASTM, B557M-10 standard. However, for building direction tensile samples same standard could not be followed due to the short build height. In this situation, customized small tensile samples were extracted along the building height so that two-layer interfacial joint strength could be tested, as shown in Fig. 3. The samples tested for this study have been taken out from the built part, and their locations are shown in Fig. 3c. The same procedure for characterization has been followed, discussed in Sect. 2.1. And finally, a functional spur gear has been cut out from the fabricated built by machining to demonstrate a 3D prismatic part fabrication strategy utilizing FSAM and machining.

3 Results and discussion

The results from this investigation have been discussed in two segments. Section 3.1 discusses the effect of different pin overlapping on the process-property relationships of AA6061-T6 alloy. It was followed by fabricating a multi-layered structure with an optimized tool pin OP in Sect. 3.2. The influence of effective pin overlap in multi-track

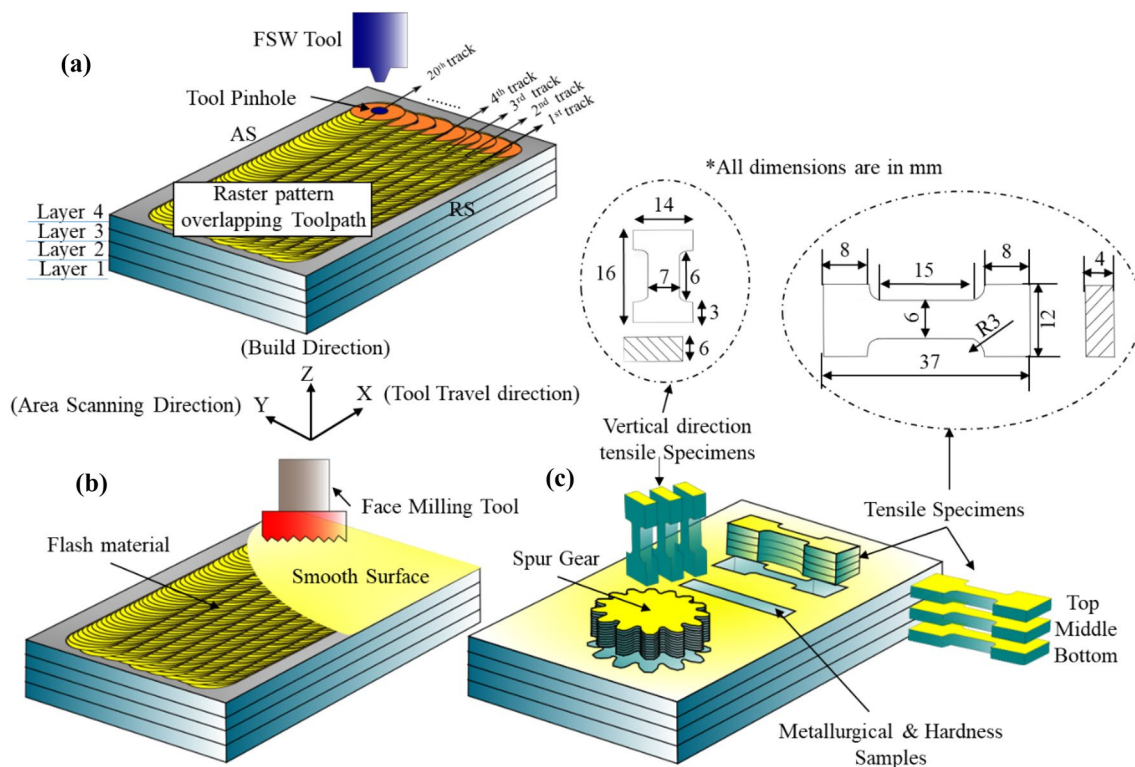


Fig. 3 a Multi-layered block fabrication by FSAM; b Face milling for smooth surface preparation; c Different positions of metallographic samples and spur gear on the built

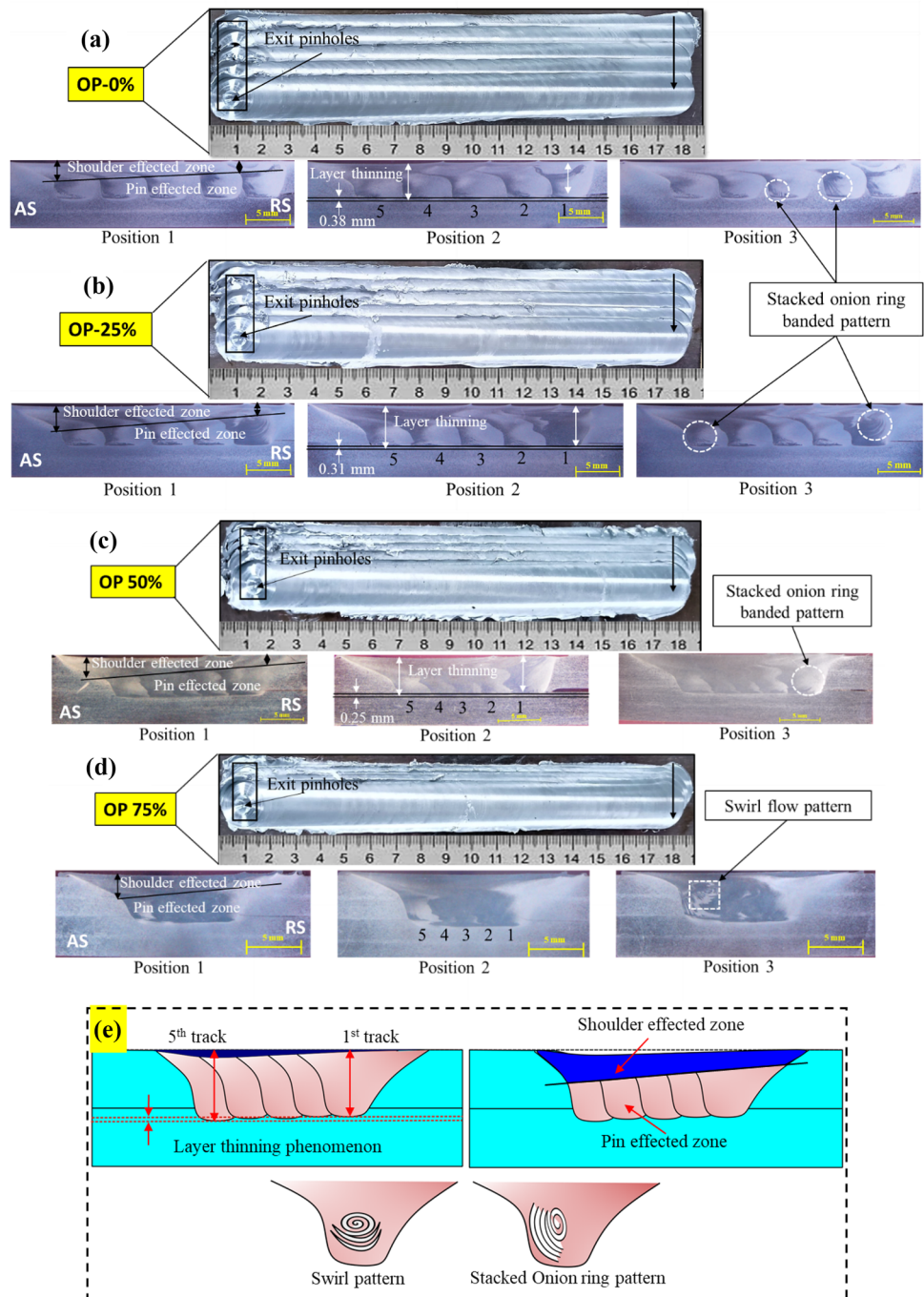
multi-layer FSAM has been discussed regarding material flow nature, microstructural, and mechanical property evaluation. The detailed discussions are presented in the following sub-sections.

3.1 Characterization of multi-track FSAM

3.1.1 Surface morphology and macrographs

Figure 4a–d show the weld surface morphology, which revealed no evidence of surface defects after two-layer joining. The cross-sectional macrographs are shown for three different locations at positions 1, 2, and 3 (Fig. 4). These macrographs give an insight into the material mixing in the SZ. As the welding tracks were performed in a unidirectional

Fig. 4 Weld surface appearance and its cross-sectional macrographs **a** 0%, **b** 25%, **c** 50%, **d** 75%, **e** layer thinning, different zones and flow patterns



raster pattern. The flash generated on the AS of the previous track has been re-stirred during the next track due to a ploughing action of the tool shoulder. Very minimal flash material has bulged out from the RS. The reason is confined to the shoulder concavity and adequate plunge depth, which restrict the flow of maximum plasticized material under the shoulder surface.

The macrographs revealed the similarity in SZ appearance for all the processed zones. But, some asymmetric flow patterns are observed at a few locations depicted by white-circled regions. Very distinct stacked 'onion ring type split patterns' are observed in 0% and 25%; such flow patterns are sporadic in the 50% overlap case. These are dark bend concentric half-ellipse-shaped patterns commonly found in the nugget zones (NZ) [13]. In this study, these patterns are more prominent in the middle and bottom parts of the stirred zones on the advancing sides of most tracks. These banded structures appeared due to the periodical deposition of the plasticized material layers [36, 37]. The material transfers in the pin-driven region take place in a layer-by-layer manner. As the pin-driven material interacts with the shoulder at the retreating side, it transfers from the retreating side to the advancing side. When the shoulder interaction increases, the shoulder and pin-driven material merge and form onion ring-type dark band structures [38].

In the case of 75% overlap, the 'onion ring type band structures' have vanished. Instead, a 'swirl-type material flow pattern' has been observed in the 5th track at position 3. This may be due to the excessive heat input as multiple tracks have been performed in a stipulated area, which results in a good intermixing of plasticized material driven by both shoulder and pin.

But a minor layer thinning incident is noticed in all cases, as overlapping weld tracks progress from the 1st track to the 5th track, as shown in Fig. 4a–c. Layer thinning is a common occurrence in the FSW process in which the thickness of the substrate is reduced by a certain amount due to the plunging of the tool shoulder and coming out of flash material from the SZ. It could be more prominent in multi-track FSAM in a progressive toolpath direction as shown in Fig. 4e. It was measured from cross-sectional micrographs using ImageJ software. It was calculated by taking the stirred zone's height difference between the first and last track. A decreasing trend of layer thinning has been found with an increase in OP due to the deposition of re-stirred material on the advancing side of the previous track. In the case of 75% overlap, no evidence of layer thinning is observed. However, the size of the SZ is smaller in this study, and the layer thinning might be observed for larger SZ. Less tool tilt may prevent this issue as tool tilt imposes an extra plunging effect on the base metal by the trailing edge of the tool shoulder. This results in a slight gap between the base plate and half of the tool shoulder on the advancing side of the previous track.

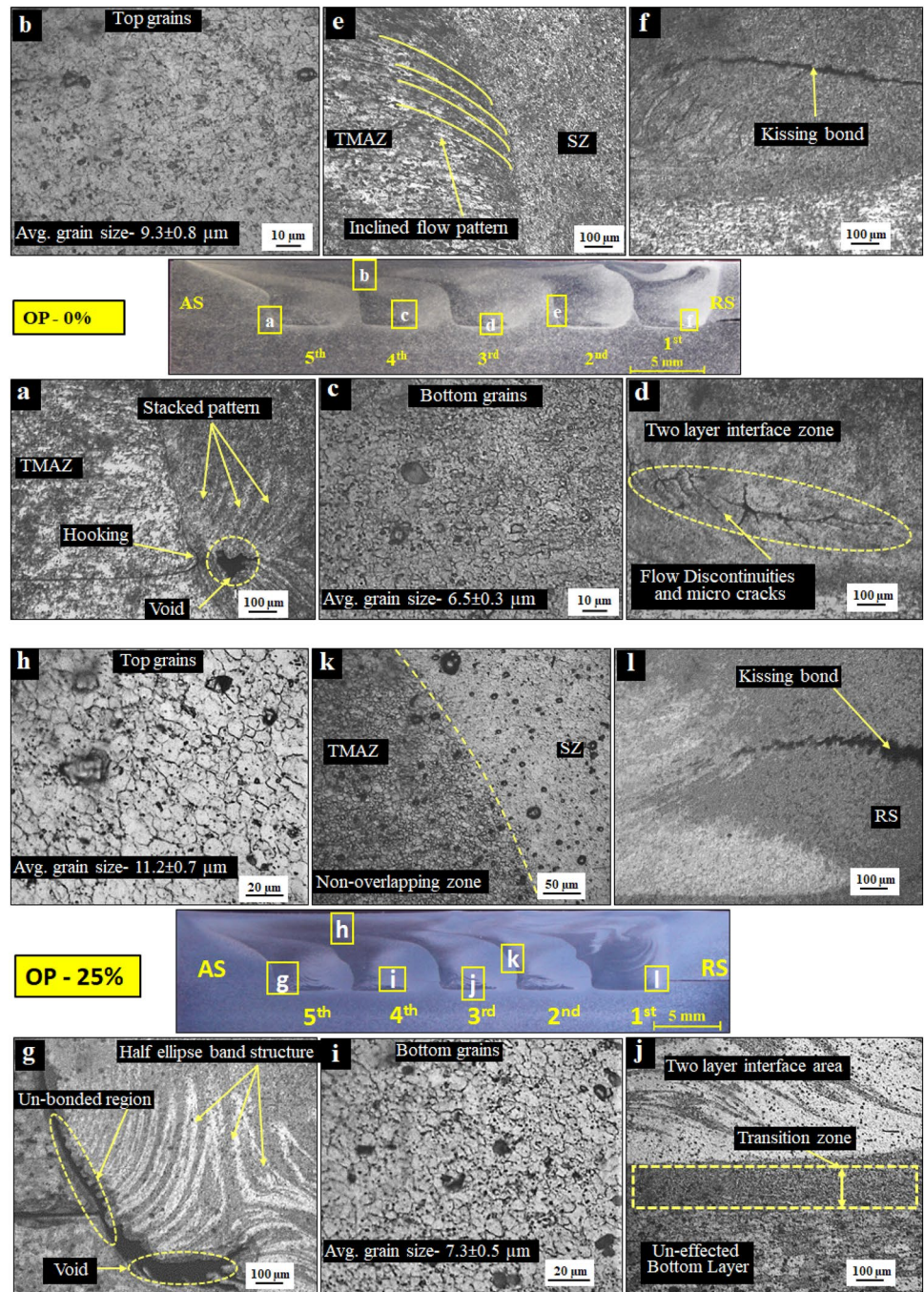
When the same plunge depth is applied for the successive tracks, it automatically takes more plunge depth on the AS of the current track. This phenomenon will continue till the last track and come up as layer thinning. More interestingly, macrographs show that the shoulder effect on the stirred zone is increased from the 1st track to the 5th track; as a result, the height of the flow arm is decreased. It is because of preheating by the precursor tracks, which is ideally suitable for better mixing and joint sound quality.

3.1.2 Microscopic observations

Figure 5a–f shows the microstructural morphology of a 0% overlap case. In Fig. 5a, the micro void has been identified, which was present on most of the tracks. It was located on AS of the SZ, near the two-layer interface, bounded by the dark band stacked patterns. This indicates the resistance to material flow from the RS to the trailing side of the tool pin, which is attributed to the minimum heat input on the void area. Moreover, it was found that some plasticized material tends to flow upward from the SZ to the thermo-mechanical affected zone (TMAZ) through the layer interface, resulting in voids formation. In the joint lap configuration, the tool pin penetrates the lower sheet, and the material extrusion gets disturbed due to the presence of oxide layers at the interface. Thus the material flow on the TMAZ appeared as inclined flow patterns that occasionally arise as the hooking defects on AS adjacent to the layer interface [32]. In Fig. 5d, some flow discontinuities and micro-cracks are observed near the interface. It may occur due to the insufficient pressure exerted by the tool shoulder. Light dark zig-zag lines are also found on RS of the first track in Fig. 5f, commonly termed kissing bonds, which occurred due to inadequate material stretching near the pin, resulting in an insufficient breakage of oxide layers near the interface [39]. In Fig. 5b, c, e, revealed the grain distribution at the top and bottom of the SZ, and non-overlapping TMAZ, respectively. The plastic deformation of material induces dynamic recrystallization that leads to refined and equiaxed grain structures [40]. But in, non-overlapping regions show coarser grains as they are on the TMAZ, which does not get sufficient heat input to reach the recrystallization phase. Moreover, the grains on TMAZ got distorted and tended to orient along the flow pattern due to shear deformation induced by the tool rotation, as shown in Fig. 5e.

Figure 5g–l shows the microstructural appearances for 25% overlap. The presence of a void defect on the 5th track on the AS of the SZ, shown in Fig. 5g, also portrays a clear separation between SZ and TMAZ. An increase in overlapping led to a smaller processing area attributed to more heat input aided in preheating the layer and enhancing the material flow in the NZ. In Fig. 5j, no micro-cracks and discontinuities are present at the bottom region on the layer

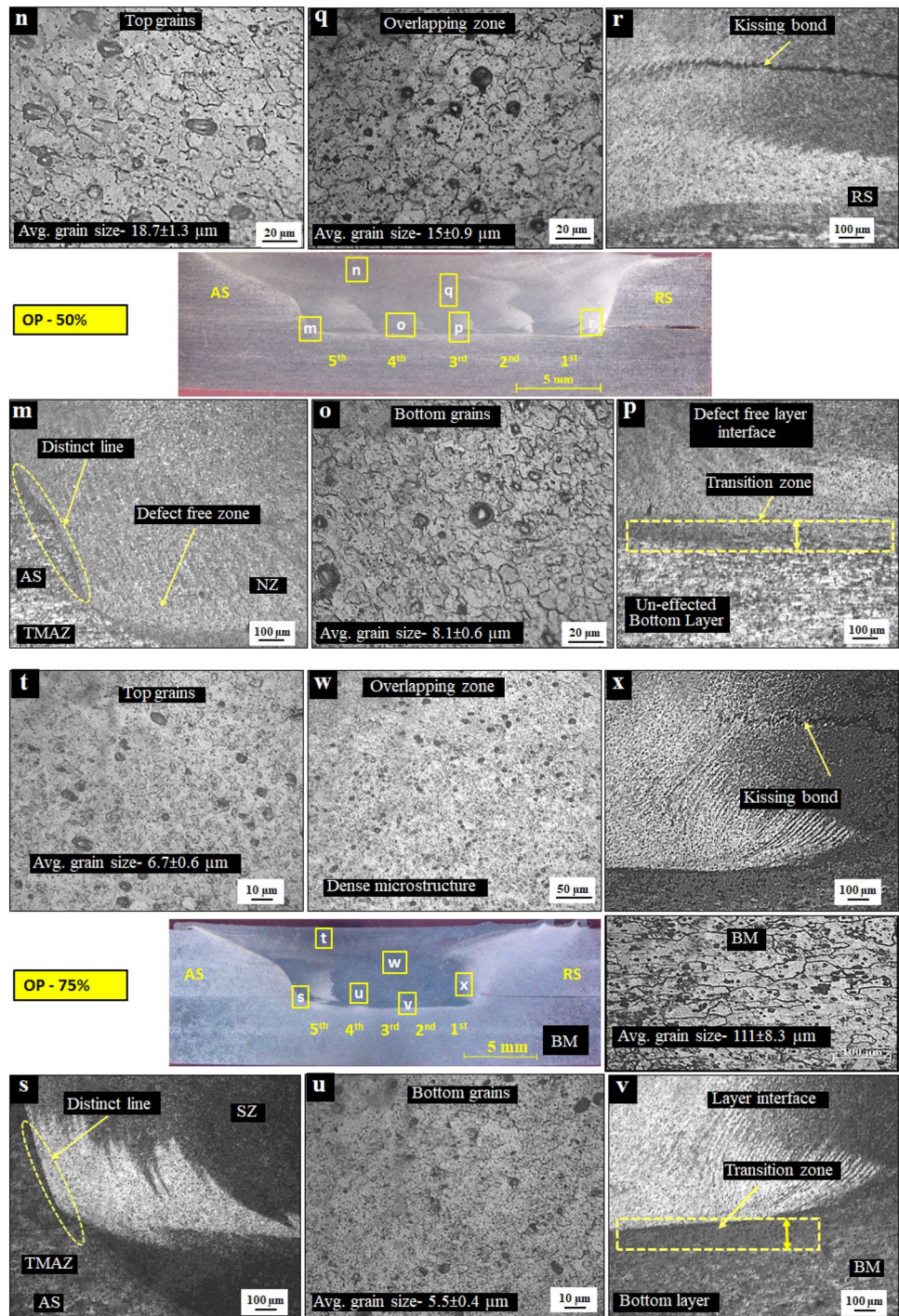
Fig. 5 Microstructural orientation in different overlapping area joining



joining interface. But Fig. 5l shows the kissing bond defect's propagation on the first track's RS. Figure 5h, i display the more refined grain distribution, and the average grains size was measured at $11.2 \pm 0.7 \mu\text{m}$ and $7.3 \pm 0.5 \mu\text{m}$, respectively. A good arrangement of grain orientation has been observed in the non-overlapping zone, as shown in Fig. 5k. This is because, with an increase in OP, successive tracks come closer to each other, and from the 2nd track onwards, every track has performed on the TMAZ of the previous track.

Figure 5m–r show the changes in microstructural level in 50% overlapping specimen. From Fig. 5m, it can be seen that no microvoids formed on the last track. Moreover, the half-ellipse-like band structures vanish, and slightly stacked patterns appear. It was reported that onion ring-type band structures disappeared when the heat input increased during the process [36]. It indicates sufficient heat input in case of 50% overlap. As the OP increases, the pin shifts towards the previous track's AS by half its diameter, which enables the re-stirring action in half

Fig. 5 (continued)



of the SZ. More of the area that comes under the tool are got re-stirred on the subsequent tracks. As a result, the region is softened enough due to the additional heat generation, which helps to adequately mix shoulder- and pin-driven material. Figure 5p shows the defect-free layer joining interface. The grain distribution is similar in the top region and overlapping area of all adjacent tracks, as shown in Fig. 5n, q. The average grain size of the top and

the overlapping regions are measured at $18.7 \pm 1.3 \mu\text{m}$ and $15 \pm 0.9 \mu\text{m}$, respectively. At the same time, the grain size at the bottom part of the NZ is estimated as $8.1 \pm 0.6 \mu\text{m}$, which is relatively less compared to the top grains. The bottom grain distribution is shown in Fig. 5o. But, like in other OP cases, a similar kind of kissing bond defect was observed on the RS of the 1st track, shown in Fig. 5r.

In Fig. 5s–x, microstructural appearances of 75% overlap have been shown, where processed zones are almost defect-free. As shown in Figs, recrystallized refined grains are identified in the top, bottom, and overlapping zones. 5(t, u, w), a dense microstructure is formed in the SZ. As the pin overlapping is relatively high, nearly the same zone is getting re-stirred multiple times. This attributes to excessive plastic deformation of the SZ material, which has led to excessive softening and thereby affected the contact pressure exerted by the shoulder. This may influence the material flow in the processing zone due to fluctuations in the contact condition between the tool with the workpiece. An alternative material flow is evident from the cross-sectional macro-graphs of three different locations. So, it can be suggested that controlling the overlapping percentage aided in achieving better material mixing and defect-free SZ. It also provides sufficient shoulder pressure for crushing the layers of oxides [39]. The kissing bond that appeared during the 1st track on the RS cannot be removed by an increase in OP, as shown in Fig. 5x. Performing an extra pass on the RS of the first track may be effective in eliminating the kissing bond.

In all levels of overlapping cases, on the AS of the 5th track, a distinct boundary is visible between the NZ and TMAZ, but the same is not evident on the RS of the 1st track. This is because, on the samples' AS, the welding direction was similar to the tangential rotational direction of the tool [41]. Notably, the TMAZ is very narrow at the bottom side of each track, resulting in a sharp transition from fine-grained SZ microstructure to coarse-grained base metal (BM) microstructure, as shown in Fig. 5j, p, v, termed as a transition zone. The average grain size of BM was 111 μm which has been substantially reduced after 1st layer joining due to dynamic recrystallization and formed equiaxed shape refined grains over the SZ. The top grains' average size increases from 0 to 50% as the overlapping area increases. This is due to the grain re-growth phenomenon during subsequent welding tracks that act as a post-heat treatment process for the previously performed tracks. As the OP increased, the weld center lines came closer, increasing the SZ's heat exposure time.

At such conditions, aluminum alloys are more susceptible to grain growth, resulting in a bimodal grain size distribution, i.e., a mixture of coarse and refined grains. The average size of bottom grains is quite similar, which may be attributed to a variation of strain rate across the SZ as overlapping increases. It is reported that grain becomes finer at higher strain rates [42]. The material deformation and grain refinement in the top region of the stirred zone are mainly controlled by the stirring action of the shoulder. As the shoulder is larger than the pin, it will generate more heat in the top region, which results in more heat input. But the pin's stirring action mainly deforms the bottom region, which results in low heat exposure. Typically, it will take

longer to dissipate the heat from the top region compared to the bottom region. It facilitates a higher cooling rate in the bottom region which reduces the nucleation time to the grain growth. This ensures the fine-grain microstructure at the bottom region. In the case of AA6061-T6, the cooling rate was mainly governed by the welding speed and ranged from 12.4 $^{\circ}\text{C}/\text{s}$ to 44.5 $^{\circ}\text{C}/\text{s}$ depending on particular welding conditions [43]. This ensures the fine-grain microstructure at the bottom region. Approximately similar grain size and distribution were observed in 75% overlap across the whole processed area due to less thermal gradient. An increase in overlapping increases heat input and induces a superior material flow, suggesting that even a simple taper tool without threads can be much more effective for large-area joining. The area of the weld nugget, the thickness of the shoulder-influenced region, and generated peak temperature are more for the taper threaded tool, irrespective of traverse speed. The torque and forces increase with the increase in traverse speed for both tools, where higher values were attained by taper-threaded tools [44].

In Fig. 6a–d, revealed the heterogeneous secondary particle distribution at the non-overlapping, partially and fully overlapping zones with varying OP. Notably, the distribution is homogeneous in nature at fully overlapping zones, which can be observed from Fig. 6c, d. The magnified images reveal the pit formation, serrated aluminum particles, and the presence of some harder particles. Moreover, the FSW process has been found to aid the fragmentation of needle-like Mg_2Si and the formation of spheroidal particles redistributing along the grain boundaries, which is also supported by Nami et al. [45]. The strength and micro-hardness of friction stir welded 6xxx series T6 conditioned alloys depend on the distribution and size of the strengthening precipitates. The precipitation sequence is very complex and depends essentially on the Mg/Si concentration ratio; it takes place in the following stages: α (supersaturated solid solution) \rightarrow GP zones or clusters of Mg and Si \rightarrow metastable β'' (coherent) \rightarrow metastable β' (semi-coherent) \rightarrow β stable phase- Mg_2Si (incoherent). The maximum hardening effect was observed mainly in the case of nano-precipitate formation [46]. FSW results in softening of the SZ, which leads to a reduction in microhardness. This is caused by the high heat input and strain rate during FSW that allows for the dissolution of β'' phase (Mg_5Si_6) precipitates which is responsible for hardening in the BM [47]. It had been reported that taper/conical pin weld produces a low density of coarser precipitates due to higher peak temperature that causes dissolution of precipitates. Many studies have proposed a similar mechanism of softening the heat-affected zone (HAZ) and TMAZ due to the dissolution and coarsening of precipitates in 6xxx series alloys [48]. The EDS analysis has performed on a 25% sample, where prominent white-colored precipitates were visible, as shown in Fig. 6e. Area scanning

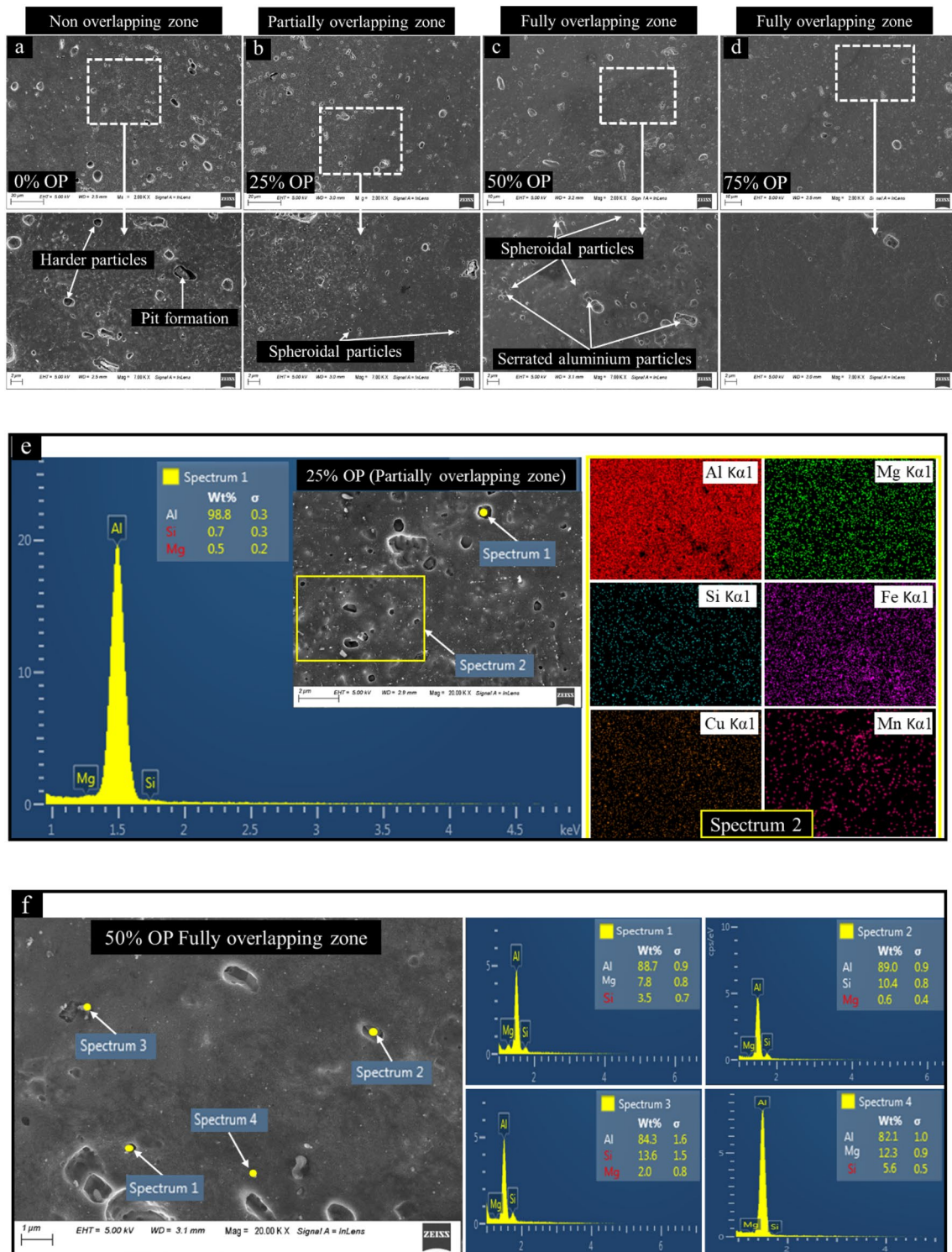


Fig. 6 FESEM images of secondary particle distribution; the EDS analysis of 25% OP and 50% OP samples

(spectrum 2) revealed non-hardening constituents such as Fe, Cu, and Mn, along with Mg/Si precipitates. The presence of Fe as an impurity in aluminum alloy results in the formation of coarse Fe and Si-rich constituents during the

elaboration of the material and does not contribute to the alloy hardening [49]. Again, EDS performed on a 50% overlapping sample, as shown in Fig. 6f, at the black spheroids (spectrum 1 & 4) revealed the probable weight % of Mg/Si

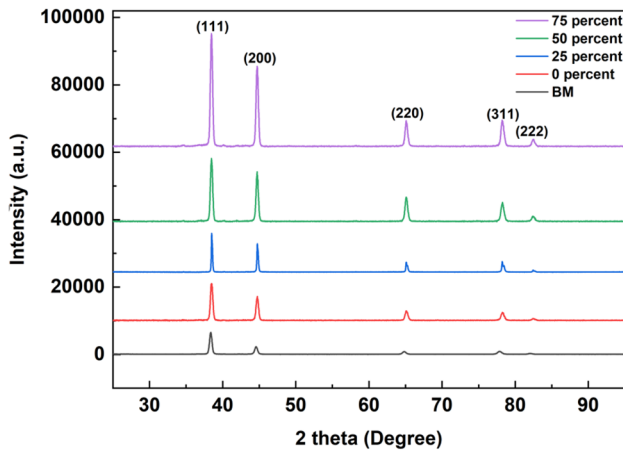
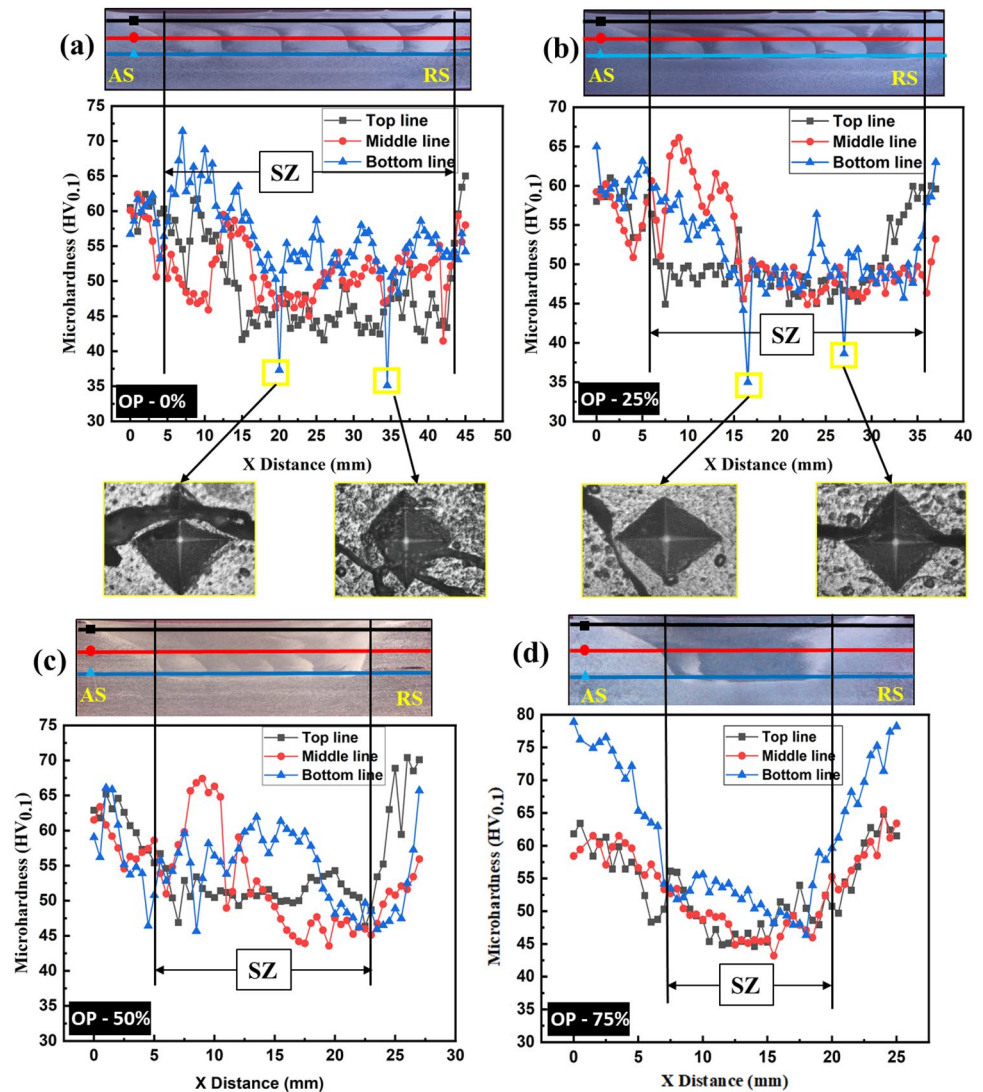


Fig. 7 Phases present in the base metal (BM); and phases formed during FSW of AA6061-T6 alloy with different OP

constituents that can support the presence of spheroidal type stable β phase Mg_2Si particles that are mainly responsible for precipitation hardening in aluminum alloys. The results of spectrums 2 & 3 (in Fig. 6f) disclose the Si-rich particles inside the pits and arbitrary-shaped whitish particles. But, the microstructural images of uniform striation showed a variation in the distribution of those black spheroid particles over the processed area due to different overlapping levels, which were manipulated by the tool stirring action along the overlapping and non-overlapping tracks.

The XRD results shown in Fig. 7 revealed that 0%, 25%, 50%, and 75% overlapping form similar phases w.r.t theta angles across the cross-sections of the processed zone. No peak shift or phase change phenomenon has been noticed, which assures that no foreign compound is present. However, the results compared with base metal revealed the increased intensity of the phases at the SZ material due to the rigorous dynamic recrystallization that happened during the overlapping tracks.

Fig. 8 Average micro-hardness distribution for 0% (a), 25% (b), 50% (c), 75% (d)



3.1.3 Micro-hardness evaluation

The average micro-hardness distribution across the SZ for different OP has been presented in Fig. 8a–d. A non-uniform average hardness distribution has been observed in all cases of overlapping. The average micro-hardness, as measured from base metal, was 84 HV_{0.1}. In the case of 0% and 25%, the hardness value drops on a few points due to indent on the micro-voids and cracks; the same is shown in Fig. 8a, b. Such incidents did not occur for the rest of the samples. The lowest hardness measured on the processed area was 35 HV_{0.1}, and the highest value was 72 HV_{0.1}.

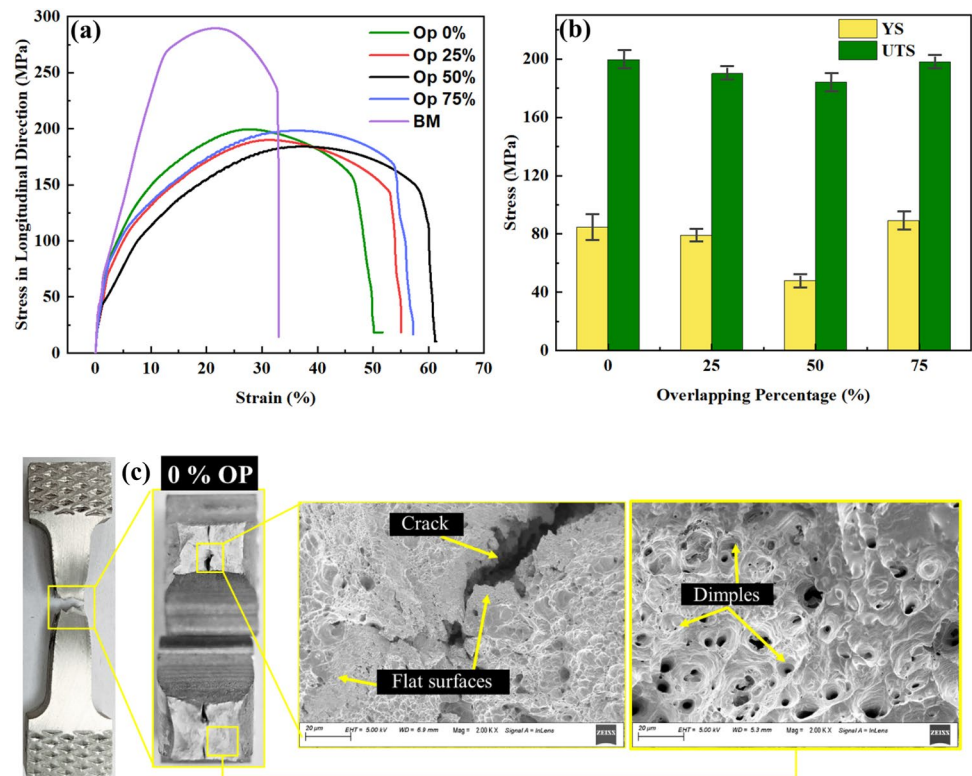
Although hardness profiles show asymmetry, middle line hardness has not shown much fluctuation compared to the other two lines. The bottom line, i.e., adjacent to the layer interface, shows more hardness value than the top and middle lines, as the smaller grain sizes were measured at the bottom section. The overall hardness of the 0% sample is higher than other overlapping samples. It was due to the grain growth phenomenon that primarily affected 25% and 50% of samples; as a result, grain size increased. And in 75% overlap, although the grain size was small, hardness still decreased, as shown in Fig. 8d. It can be attributed to the dissolution of the secondary precipitates, as the spheroidal particles were rarely found on FESEM images, as shown in Fig. 6d. However, according to the Hall–Petch relationship, the hardness value on the SZ should be higher than in other zones because of its fine equiaxed grain structure. The lower

hardness values of SZ, as compared to TMAZ, are possibly due to the thermal history of the multi-track scanning of AA6061-T6 alloy, which dissolves or coarsens the Mg₂Si precipitates across the processed area. Moreover, lowering the hardness can be analyzed by the Orowan mechanism [50], which is based on the impediment of dislocation movement around small precipitates inside grains, which may overshadow the Hall–Petch mechanism based on grain size [51]. Now, it can be stated that the average micro-hardness of AA6061-T6 alloy decrease by the raster pattern overlapping multi-track scanning strategy.

3.1.4 Tensile properties and fractography analysis

The variation in tensile strength in parallel to scanning direction as shown in Fig. 9a, b. It has been revealed that all specimens show very close peaks on the stress–strain graph. No significant variation was observed in longitudinal tensile strength with the tool pin OP. The same welding direction attributed unidirectional grain growth phenomenon irrespective of the overlapping variation. The maximum ultimate tensile strength (UTS) was achieved at 199 MPa, which is 70% of the base metal strength in the longitudinal direction. The maximum yield strength (YS) was 85 MPa for a 75% overlapping percentage. Maximum Elongation (EL) was recorded at 61% against 50% overlapping cases, and overall ELs varied between 50 to 61%. Results confirmed the strain hardening effect, which is quite significant in

Fig. 9 a Variation in stress–strain curves, b The YS & UTS in the longitudinal direction for the different OP, and c fracture surface 0% overlapping percentage



all overlapping cases than the BM (elongation 18%). That ascertains more ductile behavior of the joined area through multi-track FSAM.

To understand the failure mechanism, fractured surfaces were analyzed through SEM, and the same has shown in Fig. 9c. The failure in all OP samples was similar, following a cup and cone-type fracture. From Fig. 9c, the failure initiation point was identified as an un-joined area between two overlapping tracks that transformed into a crack. The flat flakes around the crack in the fractured surface signify the brittle fracture mode. At the same time, many irregularly shaped dimples are present in the fractured surface, indicating the combined ductile and brittle failure mode.

Figure 10a, b shows the strength variation in the transverse direction. The results revealed that 50% overlapping shows a maximum UTS of about 189 MPa, which is 68% of the base metal. The remaining 25% and 75% of specimens showed nearly the same strength, and 0% of samples showed less. Overall 50% overlapping showed better YS and more elongation, about 43%. The UTS and YS have increased with an increase in pin overlapping attributed to the enhancement of the malleable nature. In the 50% case, substantial grain growth has evident from Fig. 5n. Moreover, as revealed from SEM images, no micro-cracks or voids were found on the SZ and the homogeneous re-distribution of the secondary precipitate particles. The elongation (EL) rate varies between

33 and 43%, which has decreased as compared to the longitudinal direction specimens. It may have been attributed to the sheet rolling direction that supports the stretching of grains in the longitudinal direction; as a result, more elongation occurred. In both cases, the strain-hardening effect has noticed that acknowledged by the more ductile nature of the tested samples.

The fracture surfaces of tested samples were analyzed in SEM, as shown in Fig. 10c, d. In 50%, overlapping sample fractures that occurred from the 3rd track can be seen from the cross-sectional image, shown in Fig. 10c. Many dimples and cleavage facets were present on the fracture surface, indicating ductile–brittle mixed mode failure. But the effect of ductility was more prominent. In the case of 75%, an overlapping fracture occurred from the edge of the processed zone, which can be witnessed in Fig. 10d. The fracture surface shows more flat surfaces than dimples. The 75% OP has finer grains in the processed zone as compared to others. Generally, finer grains sharply decrease the ductility of the material, which supports the brittle failure mode. Tensile property evaluation in both directions showed that multi-track overlapping increase the overall ductility of the samples due to the strain-hardening effect on the SZ zone during the process.

In the additive process, layer delamination is critical under shear loading. The variation in tensile-shear strength

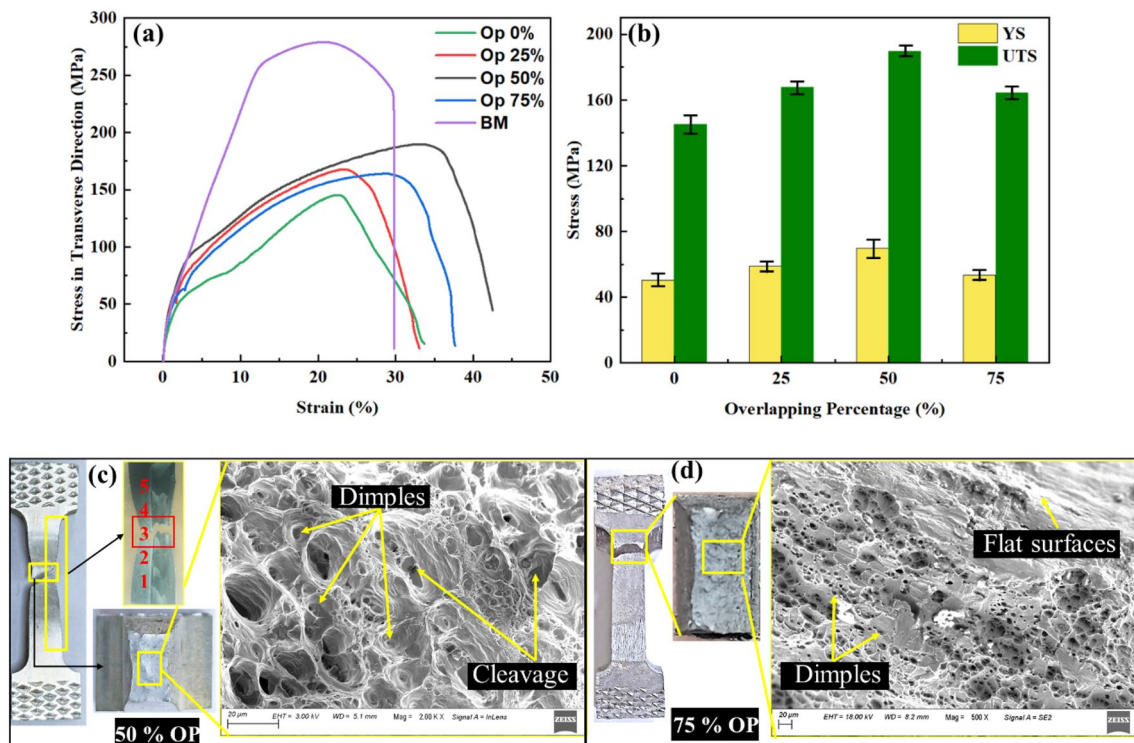
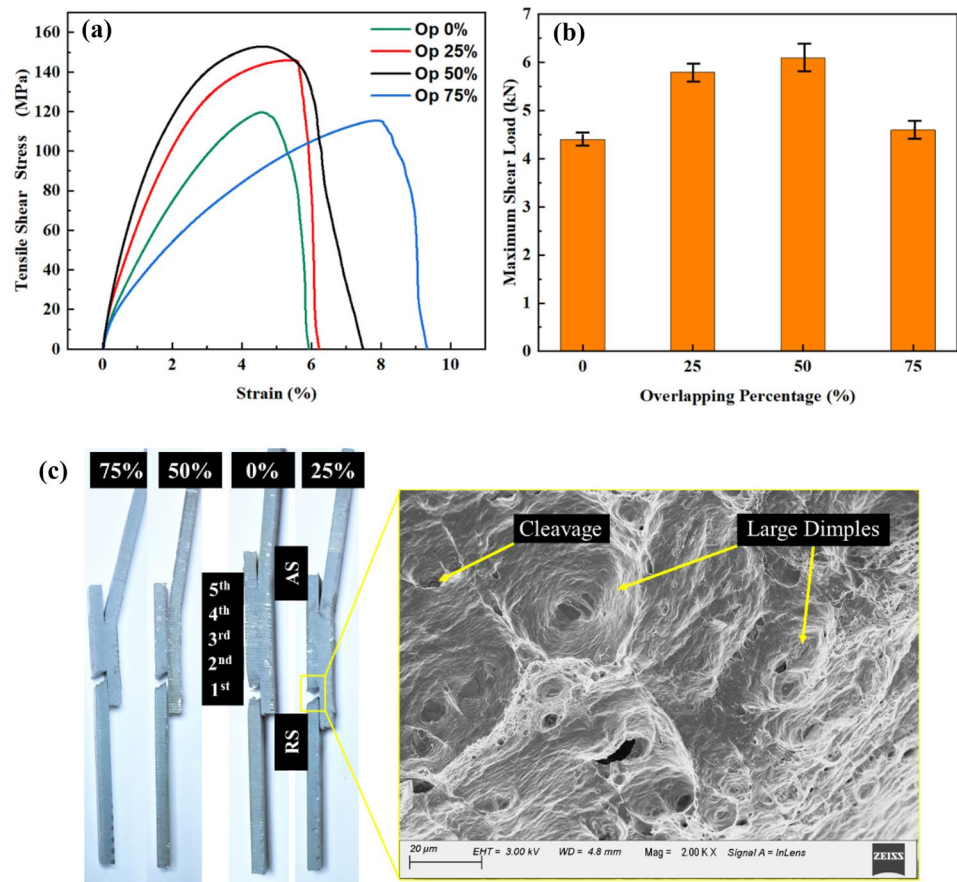


Fig. 10 a The stress–strain curves, b The YS & UTS variation; for transverse direction tensile samples for the different OP, fracture surface, and cross-section for c 50% and d 75% OP

Fig. 11 **a** Lap-shear stress vs. strain curves; **b** maximum shear loads; for different overlapping conditions; and **c** fracture locations in all samples and fractographic images



and the maximum shear load applied to the samples have shown in Fig. 11a, b. The results showed that 25% and 50% overlap exerted approximately the same strength, and 0% and 75% samples showed the same strength with maximum EL of 9% in the case of 75% overlap. At the same time, the 50% overlapping showed a maximum strength of 152 MPa, and its maximum shear load-bearing capacity before fracture was measured at about 6 kN.

Fracture locations in lap-shear tensile samples and fracture surface analysis are shown in Fig. 11c. It can be observed that all samples were fractured from the RS of the 1st track, and the crack initiation starts from the location where the kissing bond was identified at the two-layer interface, as shown in Fig. 5f, l, r, x. All fractured samples experienced some bending stress due to eccentric axial loading during testing; same can be verified from the images of fractured samples. The failure locations and modes were nearly identical in all overlapping cases. That's why only one fracture surface has been shown here in Fig. 11c. Enlarged dimples and cleavages on the fracture surface indicate a mixed failure mode in all cases.

The above discussion of varying pin overlapping can uphold that 50% overlap is more effective in terms of large-area scanning while using a cylindrical taper tool.

The processed zone was a mostly defect-free, uniform distribution of strengthening precipitates in the overlapping zones and improved mechanical properties compared to the remaining samples. So, based on these arguments, it has been intended to join multiple layers of AA6061-T6 alloy by raster/parallel pattern toolpath with 50% pin overlap.

3.2 Characterization of multi-layer multi-track FSAM

A multi-layer structure has been fabricated by multi-track FSAM using four layers of AA6061-T6 material. A unidirectional raster toolpath has been used to scan a large area, and pin exit holes are dumped at the end of each track. The layer-wise microscopic observations and mechanical testing results have shown in the following sections.

3.2.1 Material flow behavior, microstructural and mechanical property evaluation

Figure 12 reveals the material flow pattern at various locations in the case of multi-layered multi-track FSAM. Here, from the 6th track to the 14th track, has shown that similar material flow trend was observed in most overlapping

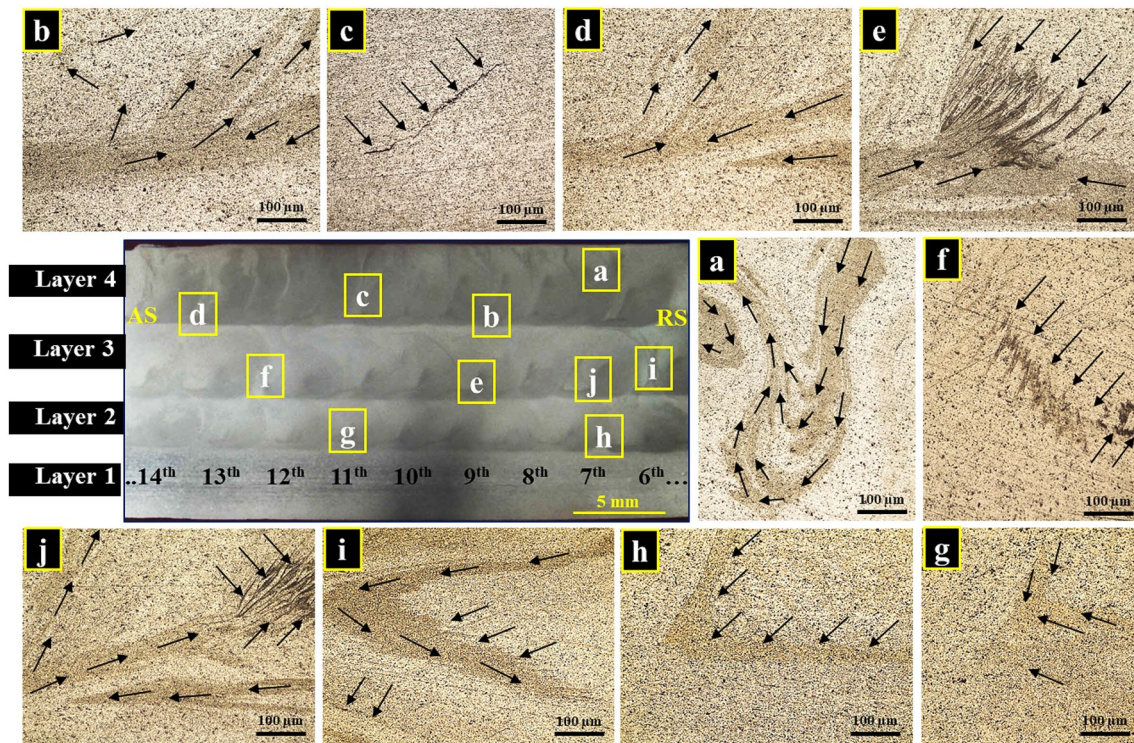


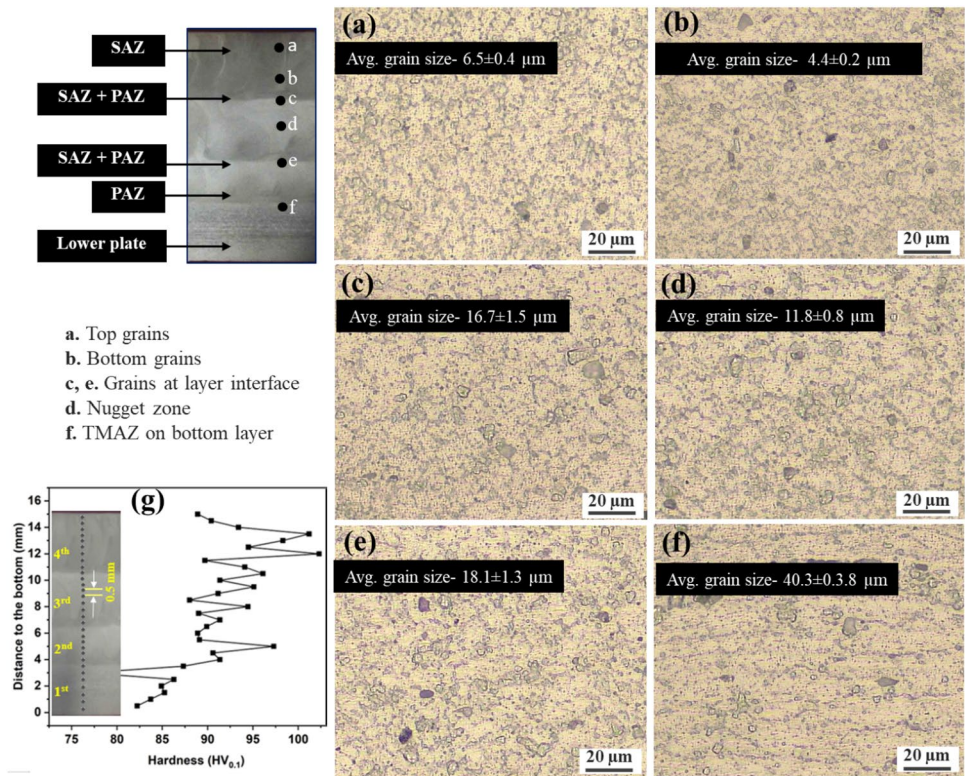
Fig. 12 Microscopic images of multi-layered FSAM built on the cross-section; (a) top layer; (b, d). Top two-layer interface; (c) top layer SZ; (e, j) 2nd & 3rd layer interface; (f, i) 3rd layer SZ; (g) 2nd layer SZ; (h) 1st & 2nd layer interface; (i) 3rd layer SZ

tracks. In the case of 50% overlap, every track has been stirred twice other than the first and last track, as the raster toolpath pattern has been followed. A better material mixing phenomenon has been noticed from the micrographs. The plasticized material starts to move from AS to the RS by the rotating action of the tool shoulder. Then it moves towards the trailing edge due to the stirring action of the pin and an axial pressure exerted by the concave tool shoulder, which restricts the material flow to escape outside from the SZ; as a result, it follows a downward movement. Then finally, return to the AS of the SZ from the bottom part, which follows an upward flow pattern, as shown in Fig. 12a. As shown in Figs, proper material mixing has been observed on two-layer interfaces. 12(b, d, h). But some stacked band structures are also noticed in Fig. 12e, j, which shows the tendency of improper material mixing at a few locations of the SZ in the case of 2nd and 3rd layer joining. Although better material mixing takes place in the SZ area (Fig. 12g), a few locations on the bottom side of the SZ have a kissing bond-like zig zag pattern that can be witnessed in Fig. 12c, f. This may be attributed to the fluctuation of shoulder pressure because of the uneven blurry surface. Moreover, due to overlapping toolpaths, the heat input is on the higher side. As a result, the tool may slip over the surface due to a reduction of the frictional coefficient. From the overall inspection, it can be stated that the multi-track multi-layered structure showed

enhanced material mixing quality in terms of reducing inherent defects. However, a dedicated defect-free area can be scanned through this strategy, which can be utilized for specific engineering applications.

In Fig. 13, different sections of the processed zone have been classified based on the FSW tool processing. The shoulder affected zone (SAZ) and pin affected zone (PAZ) can be defined as the section where the material is affected by the tool shoulder and pin, respectively. In this above built, 1st layer has only PAZ; 2nd layer has (SAZ + PAZ) on top, as this layer sustained the effect of both pin and shoulder and PAZ at the bottom; 3rd layer followed the same, and at 4th layer, SAZ at top and PAZ at the bottom. A two-layer joining interface has both zones (SAZ + PAZ). The SAZ + PAZ is the most thermo-mechanically affected zone on the built, which is exposed to heat for a longer time than the other zones. The grain distributions of different zones have been shown in Fig. 13a–f. The grain measurement reveals that grain size has decreased along the build direction. It is attributed to subsequent overlapping welding tracks and a new layer added on top. This responded to preheating the substrate and the post-heat treatment phenomenon for most processed zones in the multi-track FSAM built. It was also the reason for the grain growth phenomenon in the middle layers. On location f, the grain size was measured at $40.3 \pm 3.8 \mu\text{m}$ as it was the TMAZ of the bottom layer. At

Fig. 13 Different processed zones and grain distributions at various positions (a–f); micro-hardness distribution (g)

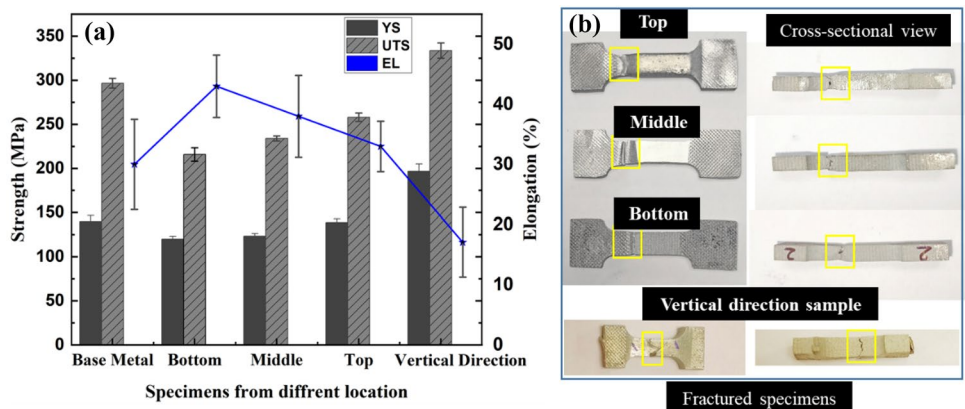


the interfaces of the 2nd, 3rd, & 4th layers, similar grain distribution and approximately the same size of grain were observed. At the top layer, the minimum grain sizes were obtained, i.e., $4.4 \pm 0.2 \mu\text{m}$ at the bottom of NZ. So, it can be considered that performing multi-layered multi-track FSAM with AA6061-T6 generates homogeneous microstructure across the processed area and accept the top and bottom-most layer.

The average hardness of the BM was measured at $84 \text{HV}_{0.1}$, as mentioned in Table 2. The average hardness distribution over the processed cross-section was found to have significantly less deviation; that's why only a one-line micro-hardness profile has been shown here. Figure 13g shows the average micro-hardness distribution along the

layer joining direction. Results revealed that the average hardness value first increased from $82 \text{HV}_{0.1}$ to $95 \text{HV}_{0.1}$ from the bottom to 5 mm, then it remained constant up to 12 mm, and afterward, a slight increment was observed. It is due to the gradual decrease of grain size with an increase in build height; the same can be observed in Fig. 13. In the case of multi-track multi-layered FSAM, the hardness property is enhanced as compared to the two layers. This may be attributed to the homogeneous distribution of the strengthening secondary precipitates due to multiple heat cycles experienced by the built. In Fig. 14a, the variation in tensile strength and EL% have been presented along the build direction, i.e., layer-adding direction. The results show that the maximum UTS was achieved at the top of

Fig. 14 Tensile strength (a), and fracture locations on tensile samples (b); along the build direction and vertical direction



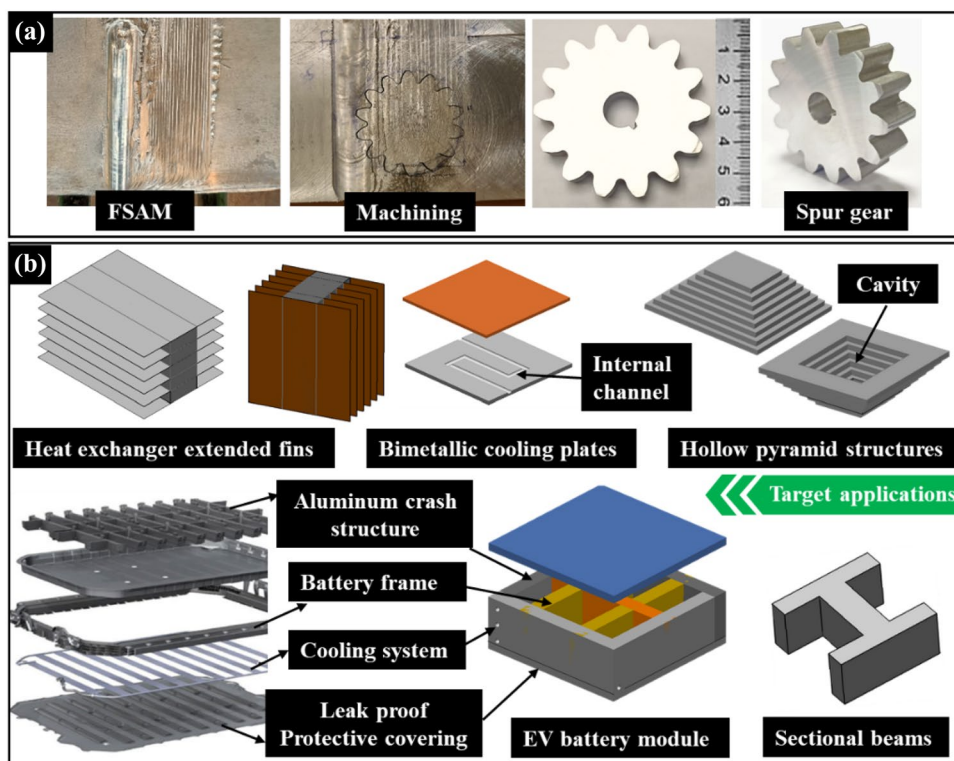
that build, i.e., 258 MPa (86.57% of base metal), followed by the middle and bottom. There is not much difference in strength between middle and bottom specimens as their grain distributions were also relatively homogeneous. Approximately the same YS values for all the specimens confirm that multiple layer joining with multi-track FSAM does not affect the YS much along the building height, as there was no change in parameters involved. Whereas the EL% shows a decreasing kind trend along the build direction as the bottom part of the built had experienced more strain hardening effect due to repetitive welding cycle, which enhances the ductility of the samples. The fractured samples show cup and cone formation during failure, which supports the ductile nature of the samples. Their factographic images have been shown on the right side of Fig. 14b. Moreover, the average tensile strength in the vertical direction shows more strength, about 333 MPa, and at the same time, EL% was measured 17%, lesser than other samples.

From the above discussion, it has been found that multi-track FSAM with 50% overlapping welding tracks enhances the mechanical and microstructural properties of the additively manufactured part. A general comparison between two-layer and four-layer built has revealed that the UTS increases with an increase in layer addition with a multi-track strategy.

3.3 Case study and relevant applications

The primary motivation behind the fabrication of a functional component is to demonstrate the enormous scope of hybridization of the FSAM process through synergistically coupled with intermediate or post-machining operations. The machining is reasonably necessary to remove flash material for a large-scale FSAM process to maintain the surface flatness for new layer addition. Similarly, machining can remove other clearances added during the layer-joining process, resulting in the realization of a three-dimensional functional component from an FSAM-built structure. There are three different build strategies (Near-net Block fabrication, Near-net Shape Fabrication via 'Form-then-Bond Approach, and Near-net Shape Fabrication via 'Bond-then-Form Approach) that can fabricate products more conveniently with less machining requirements. In this study, after fabricating a four-layered structure, a spur gear profile has been taken out from the processed zone through machining operation; all the procedures involved in this fabrication have shown a sequential manner in Fig. 15A. However, there is plenty of scope in engineering where this hybrid approach can be utilized economically with less material wastage. A few targeted applications are shown in Fig. 15B, which may find difficulties in fabrication through other AM processes.

Fig. 15 Showing a spur gear fabrication (A); Target applications areas (B)



4 Conclusions

This study investigates the effect of tool pin overlap in multiple tracks friction stir additive manufacturing (FSAM) for joining two layers of AA6061-T6 and the process–property–structure relationship of the processed region. The results from multi-track FSAM are then utilized to fabricate a four-layered block, and the built properties are evaluated. In addition, a functional component is realized from the built structure, demonstrating the FSAM and machining-based hybrid technology. The following are the summarized conclusions from this study:

- All welded surfaces were defective-free, but the cross-sections showed defects like micro cracks, voids, and material flow discontinuity in cases of 0% and 25% overlap due to insufficient overlapping of adjacent tracks. A kissing defect appeared on the RS of the first track in all overlapping cases.
- Due to overlapping tracks bi-modal grain structure was formed in the SZ. The average top grain size increased from 9.3 to 18.7 μm with an increase in overlapping up to 50% due to grain re-growth, but the average bottom grain size showed very few fluctuations. In 75% overlap, no such variation was observed as a stipulated area has been re-stirred repeatedly.
- The dissolution of secondary strengthening precipitates causes a reduction in average hardness on the SZ. Non-uniformity was observed in hardness distribution, and bottom-line hardness was high with all overlapping cases. The maximum hardness measured was 72 HV_{0.1}.
- The tensile strength in parallel to the welding direction has no significant variation. However, perpendicular to the welding direction, the samples prepared by 50% overlap showed the highest strength, i.e., 189 MPa, as the fragmented spheroidal-shaped Mg₂Si precipitates were homogeneously distributed in the overlapping zones. Fractography showed a mixed mode of failure. The 50% overlapping samples have withstood a maximum 6 kN tensile shear load.
- Successfully utilized the 50% overlap as an effective stepover for a cylindrical taper tool while fabricating a four-layered structure with multi-track FSAM revealed a dense microstructure with sufficient material mixing at the processed area.
- The transverse tensile strength and average micro-hardness increased along the build direction. The highest tensile strength was observed in the vertical direction, i.e., 333 MPa. Maximum hardness was measured on the top layer, i.e., 102 HV_{0.1}. The average grain size distribution was in close proximity to the middle layers. The average grain size at the top of the 1st and 4th layers

was measured at 40.3 and 6.5 μm . The overall mechanical properties are enhanced in the case of multi-track multi-layered FSAM.

- A spur gear was successfully realized by machining from the fabricated multi-track multi-layer block. It ascertained the feasibility of synergistic coupling of FSAM and machining to realize a 3D component.

Acknowledgements We acknowledge Technology Innovation Hub (TIH), IIT Guwahati to provide experimental facilities. We also acknowledge Department of Science and Technology (DST), New Delhi, India, for financial support for project No. SR/FST/ET-II/2017/111 (C) under Fund for Improvement of S&T Infrastructure in Universities and Higher Educational Institutions (FIST) Program.

Data availability Data related to any results in this article will be available upon request.

References

1. Ngo TD, Kashani A, Imbalzano G, Nguyen KT, Hui D (2018) Additive manufacturing (3D printing): a review of materials, methods, applications and challenges. *Compos B Eng* 143:172–196. <https://doi.org/10.1016/j.compositesb.2018.02.012>
2. Fayazfar H, Salarian M, Rogalsky A, Sarker D, Russo P, Paserin V, Toyserkani E (2018) A critical review of powder-based additive manufacturing of ferrous alloys: Process parameters, microstructure and mechanical properties. *Mater Des* 144:98–128. <https://doi.org/10.1016/j.matdes.2018.02.018>
3. Javidani M, Arreguin-Zavala J, Danovitch J, Tian Y, Brochu M (2017) Additive manufacturing of AlSi10Mg alloy using direct energy deposition: microstructure and hardness characterization. *J Therm Spray Technol* 26(4):587–597. <https://doi.org/10.1007/s11666-016-0495-4>
4. Yi S, Liu F, Zhang J, Xiong S (2004) Study of the key technologies of LOM for functional metal parts. *J Mater Process Technol* 150(1–2):175–181. <https://doi.org/10.1016/j.jmatprotec.2004.01.035>
5. Liu HJ, Hou JC, Guo H (2013) Effect of welding speed on microstructure and mechanical properties of self-reacting friction stir welded 6061–T6 aluminum alloy. *Mater Des* 50:872–878. <https://doi.org/10.1016/j.matdes.2013.03.105>
6. Vijayananth, S., Jayaseelan, V., & Kumar, N. M. High temperature superplasticity and its deformation mechanism of AA6063/SiCp. *Case Studies in Thermal Engineering*, 2019; 14, 100479. <https://doi.org/10.1016/j.csite.2019.100479>
7. Chen, Z., Li, S., & Hihara, L. H. Microstructure, mechanical properties and corrosion of friction stir welded 6061 Aluminum Alloy. *arXiv preprint arXiv:2015.1511.05507*. <https://doi.org/10.48550/arXiv.1511.05507>
8. Nezhadfar, P. D., Thompson, S., Saharan, A., Phan, N., & Shamsaei, N. Structural integrity of additively manufactured aluminum alloys: Effects of build orientation on microstructure, porosity, and fatigue behavior. *Additive Manufacturing*, 2021; 47, 102292. <https://doi.org/10.1016/j.addma.2021.102292>
9. Olakanmi EO (2013) Selective laser sintering/melting (SLS/SLM) of pure Al, Al–Mg, and Al–Si powders: Effect of processing conditions and powder properties. *J Mater Process Technol* 213(8):1387–1405. <https://doi.org/10.1016/j.jmatprotec.2013.03.009>


10. Wang Z, Wu W, Qian G, Sun L, Li X, Correia JA (2019) In-situ SEM investigation on fatigue behaviors of additive manufactured Al-Si10-Mg alloy at elevated temperature. *Eng Fract Mech* 214:149–163. <https://doi.org/10.1016/j.engfracmech.2019.03.040>
11. Tang M, Pistorius PC (2017) Oxides, porosity and fatigue performance of AlSi10Mg parts produced by selective laser melting. *Int J Fatigue* 94:192–201. <https://doi.org/10.1016/j.ijfatigue.2016.06.002>
12. Hang, Z. Y., Jones, M. E., Brady, G. W., Griffiths, R. J., Garcia, D., Rauch, H. A., ... & Hardwick, N. Non-beam-based metal additive manufacturing enabled by additive friction stir deposition. *Scripta Materialia*, 2018; 153, 122–130. <https://doi.org/10.1016/j.scriptamat.2018.03.025>
13. Tongne A, Desrayaud C, Jahazi M, Feulvarch E (2017) On material flow in friction stir welded Al alloys. *J Mater Process Technol* 239:284–296. <https://doi.org/10.1016/j.jmatprotec.2016.08.030>
14. Mishra RS, Haridas RS, Agrawal P (2022) Friction stir-based additive manufacturing. *Sci Technol Weld Joining* 27(3):141–165. <https://doi.org/10.1080/13621718.2022.2027663>
15. Rivera, O. G., Allison, P. G., Jordon, J. B., Rodriguez, O. L., Brewer, L. N., McClelland, Z., ... & Hardwick, N. Microstructures and mechanical behavior of Inconel 625 fabricated by solid-state additive manufacturing. *Materials Science and Engineering: A*, 2017; 694, 1–9. <https://doi.org/10.1016/j.msea.2017.03.105>
16. Griffiths RJ, Petersen DT, Garcia D, Yu HZ (2019) Additive friction stir-enabled solid-state additive manufacturing for the repair of 7075 aluminum alloy. *Appl Sci* 9:3486. <https://doi.org/10.3390/app9173486>
17. Avery, D.Z., Phillips, B.J., Mason, C.J.T., Palermo, M., Williams, M.B., Cleek, C., Rodriguez, O.L., Allison, P.G., Jordon, J.B., Influence of grain refinement and microstructure on fatigue behavior for solid-state additively manufactured Al-ZnMg-Cu alloy. *Metall. Mater. Trans. A Phys. Metall. Mater. Sci.* 2020; <https://doi.org/10.1007/s11661-020-05746-9>
18. Phillips, B.J., Avery, D.Z., Liu, T., Rodriguez, O.L., Mason, C.J.T., Jordon, J.B., Brewer, L. N., Allison, P.G., Microstructure-deformation relationship of additive friction stir-deposition Al-Mg-Si. *Materialia* 2019; 7. <https://doi.org/10.1016/j.MTLA.2019.100387>
19. Jordon, J.B., Allison, P.G., Phillips, B.J., Avery, D.Z., Kinser, R.P., Brewer, L.N., Cox, C., Doherty, K., Direct recycling of machine chips through a novel solid-state additive manufacturing process. *Mater. Des.* 2020; 193, 108850. <https://doi.org/10.1016/j.matdes.2020.108850>
20. Agrawal, P., Haridas, R. S., Yadav, S., Thapliyal, S., Gaddam, S., Verma, R., & Mishra, R. S. Processing-structure-property correlation in additive friction stir deposited Ti-6Al-4V alloy from recycled metal chips. *Additive Manufacturing*, 2021; 47, 102259. <https://doi.org/10.1016/j.addma.2021.102259>
21. Palanivel S, Sidhar H, Mishra RS (2015) Friction stir additive manufacturing: route to high structural performance. *Jom* 67(3):616–621. <https://doi.org/10.1007/s11837-014-1271-x>
22. Yuqing M, Liming K, Chunping H, Fencheng L, Qiang L (2016) Formation characteristic, microstructure, and mechanical performances of aluminum-based components by friction stir additive manufacturing. *The International Journal of Advanced Manufacturing Technology* 83(9–12):1637–1647. <https://doi.org/10.1007/s00170-015-7695-9>
23. He, C., Li, Y., Zhang, Z., Wei, J., & Zhao, X. Investigation on microstructural evolution and property variation along building direction in friction stir additive manufactured Al-Zn-Mg alloy. *Materials Science and Engineering: 2020; A*, 777, 139035. <https://doi.org/10.1016/j.msea.2020.139035>
24. Zhang, Z., Tan, Z. J., Li, J. Y., Zu, Y. F., Liu, W. W., & Sha, J. J. (2019). Experimental and numerical studies of re-stirring and reheating effects on mechanical properties in friction stir additive manufacturing. *The International Journal of Advanced Manufacturing Technology*, 2019; 104(1–4), 767–784. <https://doi.org/10.1007/s00170-019-03917-6>
25. Palanivel S, Nelaturu P, Glass B, Mishra RS (2015) Friction stir additive manufacturing for high structural performance through microstructural control in an Mg based WE43 alloy. *Mater Des* 65:934–952. <https://doi.org/10.1016/j.matdes.2014.09.082>
26. Zhao Z, Yang X, Li S, Li D (2019) Interfacial bonding features of friction stir additive manufactured build for 2195-T8 aluminum-lithium alloy. *J Manuf Process* 38:396–410. <https://doi.org/10.1016/j.jmapro.2019.01.042>
27. Aktarer, S. M., Sekban, D. M., Saray, O., Kucukomeroglu, T., Ma, Z. Y., & Purcek, G. Effect of two-pass friction stir processing on the microstructure and mechanical properties of as-cast binary Al-12Si alloy. *Materials Science and Engineering: 2015; A*, 636, 311–319. <https://doi.org/10.1016/j.msea.2015.03.111>
28. Nazari, M., Eskandari, H., & Khodabakhshi, F. Production and characterization of an advanced AA6061-Graphene-TiB₂ hybrid surface nanocomposite by multi-pass friction stir processing. *Surface and Coatings Technology*, 2019; 377, 124914. <https://doi.org/10.1016/j.surfcoat.2019.124914>
29. Derazkola, H. A., Khodabakhshi, F., & Simchi, A. Evaluation of a polymer-steel laminated sheet composite structure produced by friction stir additive manufacturing (FSAM) technology. 2020; *Polymer Testing*, 90, 106690. <https://doi.org/10.1016/j.polymertesting.2020.106690>
30. He C, Li Y, Wei J, Zhang Z, Tian N, Qin G, Zhao X (2022) Enhancing the mechanical performance of Al-Zn-Mg alloy builds fabricated via underwater friction stir additive manufacturing and post-processing aging. *J Mater Sci Technol* 108:26–36. <https://doi.org/10.1016/j.jmst.2021.08.050>
31. Liu F, Zhang Y, Dong P (2022) Large area friction stir additive manufacturing of intermetallic-free aluminum-steel bimetallic components through interfacial amorphization. *J Manuf Process* 73:725–735. <https://doi.org/10.1016/j.jmapro.2021.11.042>
32. Zou S, Ma S, Liu C, Chen C, Ma L, Lu J, Guo J (2017) Multi-track friction stir lap welding of 2024 aluminum alloy: processing, microstructure and mechanical properties. *Metals* 7(1):1. <https://doi.org/10.3390/met7010001>
33. Zhao, Y., Luo, Y., Lu, Y., He, Y., Guo, X., Wang, S., ... & Wang, Z. Effect of welding parameters on the microstructures and mechanical properties of double-pass aluminum/magnesium dissimilar metal friction stir lap welding joint. *Materials Today Communications*, 2021; 26, 102132. <https://doi.org/10.1016/j.mtcomm.2021.102132>
34. Al-Fadhlah KJ, Almazrouee AI, Aloraier AS (2014) Microstructure and mechanical properties of multi-pass friction stir processed aluminum alloy 6063. *Mater Des* 53:550–560. <https://doi.org/10.1016/j.matdes.2013.07.062>
35. Leitao C, Arruti E, Aldanondo E, Rodrigues DM (2016) Aluminum-steel lap joining by multipass friction stir welding. *Mater Des* 106:153–160. <https://doi.org/10.1016/j.matdes.2016.05.101>
36. Kumar, K. S. V. K., & Kailas, S. V. The role of friction stir welding tool on material flow and weld formation. *Materials Science and Engineering: 2008; A*, 485(1–2), 367–374. <https://doi.org/10.1016/j.msea.2007.08.013>
37. Gratecap F, Girard M, Marya S, Racineux G (2012) Exploring material flow in friction stir welding: tool eccentricity and formation of banded structures. *IntJ Mater Form* 5(2):99–107. <https://doi.org/10.1007/s12289-010-1008-5>
38. Geyer, M., Vidal, V., Pottier, T., Boher, C., & Rézai-Aria, F. Investigations on the material flow and the role of the resulting hooks on the mechanical behaviour of dissimilar friction stir welded Al2024-T3 to Ti-6Al-4V overlap joints. *Journal of Materials Processing Technology*, 2021; 292, 117057. <https://doi.org/10.1016/j.jmatprotec.2021.117057>

39. Zhou N, Song D, Qi W, Li X, Zou J, Attallah MM (2018) Influence of the kissing bond on the mechanical properties and fracture behaviour of AA5083-H112 friction stir welds. *Mater Sci Eng, A* 719:12–20. <https://doi.org/10.1016/j.msea.2018.02.011>
40. Pabandi HK, Jashnani HR, Paidar M (2018) Effect of precipitation hardening heat treatment on mechanical and microstructure features of dissimilar friction stir welded AA2024-T6 and AA6061-T6 alloys. *J Manuf Process* 31:214–220. <https://doi.org/10.1016/j.jmapro.2017.11.019>
41. Jayaseelan V, Jayabalakrishnan D, Muthuramalingam T, Francis Xavier J (2022) Impact of the novel square wave tool path pattern on AA6061-T6 friction stir welding. *Mater Manuf Processes* 37(8):886–895. <https://doi.org/10.1080/10426914.2021.1973028>
42. Banik, A., Saha, A., Barma, J. D., Acharya, U., & Saha, S. C. Determination of best tool geometry for friction stir welding of AA 6061-T6 using hybrid PCA-TOPSIS optimization method. *Measurement*, 2021; 173, 108573. <https://doi.org/10.1016/j.measurement.2020.108573>
43. Kalinenko, A., Kim, K., Vysotskiy, I., Zuiko, I., Malopheyev, S., Mironov, S., & Kaibyshev, R. Microstructure-strength relationship in friction-stir welded 6061-T6 aluminum alloy. *Materials Science and Engineering:2020; A*, 793, 139858. <https://doi.org/10.1016/j.msea.2020.139858>
44. Banik A, Deb Barma J, Saha SC (2020) Effect of threaded pin tool for friction stir welding of AA6061-T6 at varying traverse speeds: torque and force analysis. *Iranian Journal of Science and Technology, Transactions of Mechanical Engineering* 44:749–764. <https://doi.org/10.1007/s40997-019-00289-w>
45. Nami H, Adgi H, Sharifitabar M, Shamabadi H (2011) Microstructure and mechanical properties of friction stir welded Al/Mg2Si metal matrix cast composite. *Mater Des* 32(2):976–983. <https://doi.org/10.1016/j.matdes.2010.07.008>
46. Hakem M, Lebaili S, Mathieu S, Miroud D, Lebaili A, Cheniti B (2019) Effect of microstructure and precipitation phenomena on the mechanical behavior of AA6061-T6 aluminum alloy weld. *The International Journal of Advanced Manufacturing Technology* 102(9):2907–2918. <https://doi.org/10.1007/s00170-019-03401-1>
47. Moharami, A., Razaghian, A., Babaei, B., Ojo, O. O., & Šlapáková, M. Role of Mg2Si particles on mechanical, wear, and corrosion behaviors of friction stir welding of AA6061-T6 and Al-Mg2Si composite. *Journal of Composite Materials*, 2020; 54(26), 4035–4057. <https://doi.org/10.1177/2F0021998320925528>
48. Maji P, Nath RK, Karmakar R, Paul P, Meitei RB, Ghosh SK (2021) Effect of post processing heat treatment on friction stir welded/processed aluminum based alloys and composites. *CIRP J Manuf Sci Technol* 35:96–105. <https://doi.org/10.1016/j.cirpj.2021.05.014>
49. Maisonnette D, Suery M, Nelias D, Chaudet P, Epicier T (2011) Effects of heat treatments on the microstructure and mechanical properties of a 6061 aluminium alloy. *Mater Sci Eng, A* 528(6):2718–2724. <https://doi.org/10.1016/j.msea.2010.12.011>
50. Sato YS, Park SHC, Kokawa H (2001) Microstructural factors governing hardness in friction-stir welds of solid-solution-hardened Al alloys. *Metall and Mater Trans A* 32(12):3033–3042. <https://doi.org/10.1007/s11661-001-0178-7>
51. Rajakumar S, Muralidharan C, Balasubramanian V (2011) Predicting tensile strength, hardness and corrosion rate of friction stir welded AA6061-T6 aluminium alloy joints. *Mater Des* 32(5):2878–2890. <https://doi.org/10.1016/j.matdes.2010.12.025>

Publisher's Note Springer Nature remains neutral with regard to jurisdictional claims in published maps and institutional affiliations.

Springer Nature or its licensor (e.g. a society or other partner) holds exclusive rights to this article under a publishing agreement with the author(s) or other rightsholder(s); author self-archiving of the accepted manuscript version of this article is solely governed by the terms of such publishing agreement and applicable law.

Authors and Affiliations

Ankan Das¹ · Tanmoy Medhi¹ · Sajjan Kapil¹  · Pankaj Biswas¹

✉ Sajjan Kapil
sajan.kapil@iitg.ac.in

¹ Department of Mechanical Engineering, Indian Institute of Technology Guwahati, Guwahati, India